Revisiting dry deposition modelling of particulate matter on vegetation at the microscale

Revisiting dry deposition modelling of particulate matter on vegetation at the microscale

Tess Ysebaert[1*], Roeland Samson[2] and Siegfried Denys[1]

[1*]Sustainable Energy, Air and Water Technology (DuEL), University of Antwerp, Groenenborgerlaan 171, Antwerpen, 2020, Belgium.
[2]Laboratory of Environmental and Urban Ecology, University of Antwerp, Groenenborgerlaan 171, Antwerpen, 2020, Belgium.

Contributing authors: siegfried.denys@uantwerpen.be;

Abstract

Dry deposition is an important process determining pollutant concentrations, especially when studying the influence of urban green infrastructure on particulate matter (PM) levels in cities. Computational fluid dynamics (CFD) models of PM capture by vegetation are useful tools to increase their applicability. The meso-scale models of Zhang et al (2001) and Petroff and Zhang (2010) have often been adopted in CFD models, however a comparison of these models with measurements including all PM particle sizes detrimental to health has been rarely reported and certainly not for green wall species. This study presents dry deposition experiments on real grown *Hedera helix* in a wind tunnel setup with wind speeds from 1 to 4 m s^{-1} and PM consisting of a mixture of soot (0.02 - 0.2 µm) and dust particles (0.3 - 10 µm). Significant factors determining the collection efficiency (%) were particle diameter and wind speed, but relative air humidity and the type of PM (soot or dust) did not have a significant influence. Zhang's model outperformed Petroff's model for particles $<$ 0.3 µm, however the inclusion of turbulent impaction in Petroff's model resulted in better agreement with the measurements for particles $>$ 2 - 3 µm. The optimised model had an overall root-mean-square-error of $\sim$ 4% for collection efficiency (CE) and 0.4 cm s^{-1} for deposition velocity (v_d), which was shown to be highly competitive against previously described models. It can thus be used to model PM deposition on other plant species, provided the correct parameterisation of the drag by this species. A detailed description of the spatial distribution of the vegetation could solve the underestimation for particle sizes of 0.3 - 2 µm.

Air Quality, Atmosphere & Health
Received: 28 March 2023 / Accepted: 15 November 2023

https://doi.org/10.1007/s11869-023-01473-3

Keywords: Particle dry deposition, Size-resolved, Computational Fluid Dynamics (CFD), Model validation and optimisation, Green walls, Nature-based solutions

1 Introduction

The World Health Organisation (WHO) recently concluded that adverse health effects from exposure to PM occur at even lower concentrations than previously thought. Research on the health effects of PM exposure is complex due to the heterogeneous composition and dynamic nature of PM, as it continues to undergo chemical and physical transformations in the atmosphere. There is a consensus to classify PM by its aerodynamic diameter, because it determines transport and removal processes, into fine PM ($PM_{2.5}$) and coarse PM (PM_{10}) with an aerodynamic diameter smaller than 2.5 and 10 µm, respectively. The updated air quality guidelines by the WHO recommend a reduction of the annual averages from 10 to 5 µg m^{-3} for $PM_{2.5}$ and from 20 to 15 µg m^{-3} for PM_{10}. The 24-hour limits with a permissible exceedance of 3 - 4 days per year were also reduced, albeit to a lesser extent. Inhaling high levels of PM above the WHO limit values can lead to cardiovascular disease, respiratory diseases, and cancer, leading to premature deaths (EEA, 2022; WHO, 2021). In addition, exposure to ultrafine PM ($PM_{0.1}$) (< 0.1 µm) is a concern, as it is primarily related to combustion processes that surround us all. Moreover, they are much more toxic than larger PM fractions, since these ultrafine particles can penetrate the respiratory tract with high efficiency and are carrying greater amounts of harmful metals and organic compounds due to their higher specific surface area (Kwon et al, 2020; WHO, 2021). Urban green infrastructure (UGI) has been proposed as short-term strategy against PM pollution opposed to long-term PM emission reductions in urban settings. Large available wall

area makes green walls easier to implement in cities than other forms of UGI, such as trees and shrubs. Green walls, opposed to green roofs, are located right next to traffic, which is one of the main sources of $PM_{0.1}$ (Kwon et al, 2020) and a significant source of $PM_{2.5}$ and PM_{10} emissions (EEA, 2022). Furthermore, they do not aggravate air quality such as can be seen for trees in street canyons (Abhijith et al, 2017; Janhäll, 2015; Tomson et al, 2021; Ysebaert et al, 2021). Important in the deposition potential of a green wall is the vegetation-wind interaction. The aerodynamic effect is mainly related to vegetation density and leaf morphological characteristics (Huang et al, 2013; Koch et al, 2019; Ysebaert et al, 2022). In addition, PM deposition is determined by the leaf surface properties, e.g. presence of trichomes, leaf-wax content or chemical composition and structure of the epicuticular wax (Leonard et al, 2016; Muhammad et al, 2019; Paull et al, 2019). A distinction is made between the transfer of a particle from an air stream to a solid surface with (wet) and without (dry) the aid of precipitation. Dry deposition is governed by gravity, Brownian motion, direct interception and impaction, and its magnitude depends on the particle's properties. Ultrafine particles ($PM_{0.1}$) undergo deposition mainly by Brownian diffusion, but this process becomes negligible for particles greater than 1 µm. Interception and impaction become evident for fine and coarse PM, while sedimentation becomes dominant for particles larger than 8 µm. None of the particle capture mechanisms is efficient for particle sizes between 0.1 and 2 µm (Beckett et al, 2000; Pryor et al, 2008).

The study of dry particle deposition is of great importance, because it is a continuous process that determines pollutant concentrations and is therefore an important aspect in air quality modelling. A key concept is the deposition velocity, v_d (m s^{-1}), and is defined as the ratio of the pollutant flux towards the surface and the atmospheric particle concentration. Many studies have investigated the numerical modelling of dry deposition on UGI and the models are mainly based on the model described by Zhang et al (2001) (Hashad et al, 2023; Lin et al, 2012; Steffens et al, 2012; Tong et al, 2016)

or the model described by Petroff and Zhang (2010) (Amicarelli et al, 2021; Katata et al, 2014; Šíp and Beneš, 2017; Steffens et al, 2012). Although these models were developed for larger forest canopies at the meso-scale level, they have been adopted for micro-scale models as well. Steffens et al (2012) compared both models with $PM_{0.1}$ measurements behind a row of trees near the road and found better agreement with the Zhang et al (2001) model. Nonetheless, both models showed substantial deviations for particle sizes below 50 nm and even more discrepancies were observed when the flow field was not well resolved. On the other hand, including turbulent impaction in the Petroff and Zhang (2010) model resulted in better agreement with wind tunnel measurements for particle sizes between 0.1 and 1 µm (Šíp and Beneš, 2017). This demonstrates that a comparison of the models over a wide particle size range is needed to improve pollutant dispersion models. Hereto, wind tunnels are valuable setups for validation data. Current wind tunnel experiments used PM surrogates like salt (Ould-Dada, 2002; Beckett et al, 2000; Freer-Smith et al, 2004) or oil droplets (Shen et al, 2022), or they only looked at $PM_{0.1}$ generated with a flame (Lin et al, 2012; Hwang et al, 2011; Huang et al, 2013). Moreover, most research has focused on tree species and the PM reducing potential of green wall species remains unknown. This study presents dry deposition experiments on the climbing species *Hedera helix* in a wind tunnel setup that could generate wind speeds from 1 up to 4 m s^{-1}, corresponding to Beaufort classes 1 to 3, and to which lab-scale generated PM was added. The PM consisted of a mixture of soot particles, produced by a combustion process in the range 0.02 to 0.2 µm, and Arizona fine test dust with a particle size between 0.3 and 10 µm. The particle concentrations and particle size distribution were varied. This wind tunnel study is one of the few that examines PM deposition on vegetation of all particle size ranges important in health studies, namely from 0.01 to 10 µm. In this way, relationships could be established between the amount of deposition and particle size, fine dust concentration, type of particulate matter (soot or sand), wind

speed and relative humidity. Second, the dataset was used to compare the often cited models of Zhang et al (2001) and Petroff and Zhang (2010) so that the models are validated for a more complete PM size range. Moreover, from previous research (Ysebaert et al, 2022), the optimised drag parameters describing the complex vegetation-wind interaction were introduced and revalidated. This ensured that model errors were not propagated to the dispersion model. In the end, an optimised dry deposition model was proposed including the best features of the models of Zhang et al (2001) and Petroff and Zhang (2010). With this optimised model, we will be able to better estimate how to implement green walls and, by extension, other forms of UGI in the city to address problematic PM levels.

2 Materials and methods

2.1 Wind tunnel experiments

2.1.1 Setup

PM deposition was investigated in an open-circuit wind tunnel with a square test section of 0.5 x 0.5 m^2 and a length of 1 m (Figure 1). At both sides of the test section a diffuser was placed going from a square to a circular pipe of 0.315 m. The upwind end of the wind tunnel was connected to the outdoor air, with an intermediate region housing a honeycomb and screens, situated between the test section and the inlet. An hexagonal honeycomb with a cell length-to-diameter of 9.4 and a porosity of 0.9944 (Corex Honeycomb, Encocam Ltd) was introduced in the wind tunnel to straighten the flow. Stainless steel woven mesh screens (Omnimesh) with cell sizes of 0.1 mm were placed at both sides of the honeycomb, and a finer mesh with 0.055 mm cell size behind the honeycomb, to improve axial flow uniformity. The upwind end of the test section was connected to an extraction ventilator (MPS 355 EC 30, Ruck) that pulled air through the test section. Three different wind speeds were investigated and were

obtained by changing the flow rate of the ventilator and comparing the wind speed at the inlet of the test section. The in- and outlet were facing away from each other to prevent mixing of the in- and outlet flows. The selected free stream wind speeds were 1.1, 2.2, and 4.3 m s^{-1}, falling in the middle of Beaufort wind speed classes 1 to 3, respectively (Dulbari et al, 2017) (Table 1). During the experiment, wind speed was measured at the in- and outlet of the test section in both the y- and z-direction with a hot wire anemometer (PCE-009, PCE Instruments) which had a measuring range from 0.02 to 20.0 m s^{-1} with an accuracy of 5%. The log-Tchebycheff traverse, consisting of 7 points, was used to obtain the mean wind speed (Legg, 2017).

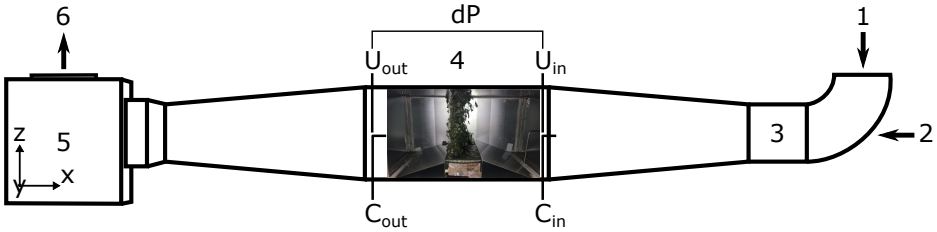

Fig. 1 Open-circuit wind tunnel setup with 1, the inlet connected to the outside, 2, the inlet of lab-scale generated PM, 3, the honeycomb-screen combination, 4, the test section, 5, the extraction ventilator and 6, the outlet of the wind tunnel to the outside. The measurement points are also shown with, dP, the differential pressure, U_{in} and U_{out}, the in- and outgoing wind speed measured with a hot wire anemometer at different heights, and C_{in} and C_{out}, the in- and outgoing PM concentration measured with an optical particle sizer and a scanning mobility particle analyser.

Table 1 Overview of the wind speeds and their associated Beaufort scale at which PM deposition was tested. The effect on vegetation for each Beaufort scale is also provided (Dulbari et al, 2017).

Beaufort number	Description	Beaufort wind speed (m s^{-1})	Effect
1	Light air	0.3 - 1.5	Smoke drifts, leaves are motionless
2	Light breeze	1.6 - 3.3	Leaves rustle
3	Gentle wind	3.4 - 5.4	Leaves and small twigs in constant motion

Lab-scale generated PM was inserted in the wind tunnel at location 2 on Figure 1. To investigate a broad range of particle sizes, a miniCAST Real Soot Generator (5201 Type C, Jing AG) and a Dust Aerosol Generator (3410U, TSI Incorporated) were

simultaneously employed to generate ultrafine particles (UFP) and fine and coarse PM, respectively. PM concentration and size distribution were detected with a scanning mobility particle sizer (SMPS) (3938, TSI Incorporated) for a particle size range of 0.01 to 0.3 µm and an optical particle sizer (OPS) (3300, TSI Incorporated) for particles with a size between 0.3 and 10 µm. The same measurement locations as for the wind speed were used. A miniCAST generated soot particles by propane (C_3H_8) combustion that takes place through oxidation at the flame front. The generated particles are consequently quenched and stabilised by a continuous flow of N_2 gas and diluted with compressed air. It has been demonstrated that generated soot can be used as a surrogate for real-world soot particles, because of its black carbon content matching with engine exhaust soot (Maricq, 2014; Moore et al, 2014; Saffaripour et al, 2017). Different particle size distribution (PSD) were obtained by changing the flow rate of the quenching gas N_2. The particle concentration was dependent on the N_2 flow rate and the applied flow rate in the wind tunnel setup, since it determined the amount of dilution. Three different miniCAST settings, designated as a, b, c, were tested and they differed in the particle mean diameter and concentration (Table 2). It can be seen that the particle mean diameter of the three settings decreased from setting a to c, and, therefore, it was decided to retain the particle diameters of each setting with the highest PM concentration to obtain a single dataset for soot. It can be observed from Table 2 that setting b and c correspond with the characteristics of typical diesel particles, namely agglomerates consisting of mainly spherical primary particles of around 0.015 – 0.040 µm (Burtscher, 2005). A dust aerosol generator (3410U, TSI Incorporated) was used to generate PM with a particle diameter larger than 0.3 µm. The device makes use of a nozzle that is fed with tiny amounts of the powder via a rotating ring and subsequently disperses and de-agglomerates the powder into a carrier air stream directed to the wind tunnel. Arizona fine test dust, A1 Ultrafine (fiatec - Filter & Aerosol Technologie GmbH) was used as a representative for urban PM. The

test dust was already used to study filter performance following ISO standard 12103 (12103-1, 2016). Three different particle concentrations were generated, namely 50, 100 and 150 µg m^{-3}. These were also designated as setting a, b and c, since they were added to the wind tunnel air flow together with the soot particles of the matching miniCAST setting. This was justified, because the PSD of both generators did not overlap. 50 µg m^{-3} was chosen as lowest concentration, since it is the previous daily mean threshold value reported by the WHO (recently updated to 45 µg m^{-3}) (WHO, 2021). The higher PM_{10} concentrations were selected to study the impact of elevated concentrations on the deposition process.

Table 2 The three test settings investigated with each a different particle size distribution (PSD) for $PM_{0.1}$ and PM_{10} generated with the miniCAST (5201 Type C, Jing AG) and Dust Aerosol Generator (3410U, TSI Incorporated), respectively, with each a specific mean particle concentration, N (cm^{-3} or µg cm^{-3}) and mean particle diameter, $\bar{d_p}$ (µm) for all three Beaufort classes under study.

Beaufort	Setting	$\bar{d_p}$,$PM_{0.1}$ (µm)	N,$PM_{0.1}$ (cm^{-3})	$\bar{d_p}$,PM_{10} (µm)	N,PM_{10} (µg cm^{-3})
1	a	0.109 ± 0.001	(6 ± 1)e^5	2.9 ± 0.1	51.12 ± 0.09
2	a	0.107 ± 0.008	(3.3 ± 0.6)e^5	2.8 ± 0.1	49.83 ± 0.07
3	a	0.104 ± 0.008	(1.1 ± 0.2)e^5	3.7 ± 0.1	58.3 ± 0.1
1	b	0.055 ± 0.004	(10 ± 3)e^5	2.9 ± 0.1	129.4 ± 0.2
2	b	0.052 ± 0.004	(4 ± 1)e^5	2.9 ± 0.1	109.7 ± 0.1
3	b	0.049 ± 0.002	(1.8 ± 0.4)e^5	3.75 ± 0.08	121.2 ± 0.1
1	c	0.032 ± 0.001	(2.8 ± 0.7)e^6	3.3 ± 0.1	179.8 ± 0.3
2	c	0.030 ± 0.003	(2.0 ± 0.3)e^6	3.60 ± 0.09	155.2 ± 0.2
3	c	0.028 ± 0.004	(2.8 ± 0.6)e^6	3.9 ± 0.1	163.8 ± 0.3

2.1.2 Treatments

The different treatments are related to the filling of the test section, the wind speed in the wind tunnel and the particle generators' settings. *Hedera helix* (common ivy), was grown in a planter of 0.2 x 0.5 x 0.1 m^3 and was attached with steel wire to a trellis of 40 mm mesh size and 4 mm rod diameter ensuring a homogeneous coverage (Figure 2, left). The planter was placed in the middle of the plants section and ramps were installed to guide the flow through the vegetation (Figure 2, right). The same planter with *H. helix* was used for all experiments and it was subjected after each experiment

to a constant air flow without addition of PM to remove easily detachable particles from the leaf surfaces.

Fig. 2 Left: Detailed picture of *H. helix* facing the air stream in the wind tunnel setup, illustrating the realistic arrangement of the climber (in terms of coverage and growth depth). Right: the planter grown with *H. helix* in middle of the test section with ramps guiding the air flow at both sides.

The leaf area density (LAD) (m^2 m^{-3}) was determined to account for the vegetation in the airflow model. To this end, leaf area (LA) was measured for 10 randomly selected *H. helix* leaves with a leaf area meter (Li-3000, LiCor Biosciences) and amounted to $(28.8 \pm 0.1) \cdot 10^{-4}$ m^2. LAD was subsequently calculated as: $LAD = LA \cdot N \cdot V^{-1}$ with LA, leaf area (m^2) , N, the number of leaves and V, the volume of the vegetation, which is set equal to the volume in line with the planter (0.2 x 0.5 x 0.4 m^3). It resulted in an LAD of 12.3 ± 0.1 m^2 m^{-3}. In addition, pictures were taken with a Canon Eos 500D camera and processed with ImageJ (version 1.53K) to calculate the characteristic obstacle length, l (m), a parameter that is required in the deposition model. For broadleaves, the obstacle length equals the leaf width (Petroff et al, 2009) and was 3 ± 2 cm for *H. helix*.

2.1.3 Data analysis

The measured concentration (C) of particles of a given diameter (i) averaged along the traverses at the entrance and exit of the test section of the wind tunnel, was used to calculate a collection efficiency, collection efficiency (CE). This is the difference between the incoming and outgoing PM concentration, normalised by the incoming

concentration (eqn. 1) for a particular particle size i. The calculated CE was used in a linear mixed model (LMM) to analyse the influence of *H. helix* compared to an empty wind tunnel on the measured particle concentration. The test case (planter without or with *H. helix* inside), the incoming wind speed (U), the incoming relative humidity (RH), the incoming particle concentration and the source of the particles (miniCAST or Dust Aerosol Generator) were set as fixed effects and one particular run as random effect to account for unmeasured environmental conditions. Before running the LMM test, outliers were detected based on a standardised score. Outliers with a standardised score (in absolute value) greater than 4, a strict threshold required for large datasets (Hair et al, 2014), were removed from the dataset. Non-significant interactions between the fixed factors were found using the Akaike Information Criterion (Sakamoto et al, 1986) and then removed from the model. In addition, a corrected collection efficiency (CE_{cor}) was calculated to obtain only the influence of vegetation on an airflow enriched with PM. It thus corrects for the amount of PM deposition on the walls of the wind tunnel and the empty planter by subtracting the collection efficiency of the empty wind tunnel from the incoming concentration measured with *H. helix* in the test section and is referred to as a corrected incoming PM concentration ($C_{in,cor}$). With $C_{in,cor}$, CE_{cor} was calculated in a similar manner to CE for a given particle diameter (i) averaged along the traverses at the entrance and exit of the test section (eqn. 2). Relationships between the incoming RH, PM concentration, wind speed and CE_{cor} were sought with another LMM study. $C_{in,cor}$ was used as input to the dispersion model, as the deposition of PM on the wind tunnel walls was not included in this model.

$$CE_i = 1 - \frac{C_{i,out}}{C_{i,in}} \tag{1}$$

$$CE_{i,cor} = 1 - \frac{C_{i,out}}{C_{i,in} \cdot (1 - CE_{i,empty})} = 1 - \frac{C_{i,out}}{C_{i,in,cor}} \quad (2)$$

Many studies report PM deposition to vegetation in terms of a deposition velocity (v_d) (m s^{-1}). It was computed following Hwang et al (2011) with the obtained CE_{cor}, the incoming air flow rate, Q_a (m^{-3} s^{-1}), LA (m^2), leaf area of a *H. helix* leaf, and N, the total number of *H.helix* leaves as follows:

$$v_{d,i} = \frac{Q_a}{LA \cdot N} \cdot CE_{i,cor} \quad (3)$$

Both the corrected collection efficiency and deposition velocity will be compared with the output of a 3D dry deposition model, which is outlined in the next section.

2.2 Numerical model

2.2.1 Air flow model

Air flow in the wind tunnel setup was modelled with the 3D incompressible, steady Reynolds-averaged Navier-Stokes (SRANS) equation together with the continuity equation using the Wilcox revised k-ω turbulence model for the Reynolds stress tensor (Wilcox, 2008) with the Boussinesq eddy viscosity assumption (i.e. linear relation between the Reynold stresses and the mean strain rate tensor). The equations were computed with a finite element method using Comsol Multiphysics™(version 6.1). The flow conditioners were included in the model by adapting the momentum and/or turbulence equations. The pressure drop created by the honeycomb was represented by the Darcy-Forchheimer relation (Mattis et al, 2012) and the parameters were obtained from pressure-velocity measurements across the section of the flow conditioners. This methodology was already applied and validated for filter layers in a CFD

model (Roegiers and Denys, 2019; Ysebaert et al, 2022). The hydraulic permeability and Darcy-Forchheimer parameter were $2.01{\cdot}10^{-6}$ m^2 and 10 m^{-1}, respectively. The screens were assumed in the model as surfaces since their width is small compared with the resolved length-scales of the flow field. Empirical relations derived for square meshes were used that link the screen's resistance to its porosity and the screen's attenuation of the turbulence kinetic energy to a dimensionless refraction coefficient, which in turn is related to its resistance (Roach, 1987).

Additional terms were added to these equations at the wind tunnel section with vegetation. The effect on air flow of the introduced vegetation in the wind tunnel was modelled by considering both viscous forces (viscous drag, represented by the permeability (K)) and pressure forces (form drag, represented by the sectional drag coefficient (C_d)) created by the vegetation elements. Both drag forces give rise to a momentum sink, S_u, defined in equation 4). To this end, vegetation was regarded as a uniform, porous medium and its effect on fluid flow was modelled on average for this volume. The amount of vegetation was introduced as leaf area density (LAD, m^2 m^{-3}), which is the one-sided leaf area per unit volume. In addition, the drag force created by plants gives rise to source and sink terms in the k and ω equations, which come with additional model coefficients which need to be defined carefully (Zeng et al, 2020). The assumptions of Sogachev (2009) were assumed, given in equations 5 and 6, for the vegetation terms in k and ω, respectively.

$$S_{\boldsymbol{u}} = -\frac{\mu}{K}\boldsymbol{u} - \rho LADC_d U\boldsymbol{u} \tag{4}$$

$$S_k = 0 \tag{5}$$

$$S_\omega = -\rho LADC_d C_{\omega 5} \beta_d U \omega \tag{6}$$

with $\boldsymbol{u}$ (m s^{-1}), the wind velocity vector (vectors are shown in bold in the equations provided in this article), U (m s^{-1}), the spatially averaged wind speed ($U = (u_i u_i)^{0.5}$), μ (Pa s), the dynamic viscosity, ρ, the air density (kg m^{-3}), LAD (m^2 m^{-3}), the leaf area density, K (m^2), the permeability of the plant material, and C_d, the average sectional drag coefficient. The vegetation specific model constants $C_{\omega 5}$ and β_d were $(0.52 - \beta)$ and 1, respectively. β is a model constant of the k-ω model itself. This vegetation model was used by Ysebaert et al (2022) to find K and C_d of three climber species with a parameterisation study linking the modelled output with experimentally determined pressure-velocity data for a wide range of mean wind speeds from 0.04 ± 0.01 to 3.81 ± 0.04 m s^{-1} corresponding with Reynolds numbers from $3{\cdot}10^3$ up to $2.5{\cdot}10^4$. The obtained relationship between K or C_d for *H. helix* with a LAD of 13.31 ± 0.01 m^2 m^{-3} was used, since it approximates *H. helix* of this study. The resulting values of K and C_d are given in Table 8 (Appendix A) and were calculated with the mean wind speed approaching the plants. This wind speed was calculated from the measured mean wind speed at the entrance of the test section (U_{in} on Figure 1), assuming a constant flow rate. The temperature (T) and RH of the incoming air flow are also provided in Table 7 (Appendix A). It is observed that K approximated the dynamic viscosity of air and, therefore, viscous drag was negligibly small compared with form drag for all investigated Beaufort classes.

2.2.2 Particle dispersion

Particle dispersion in the wind tunnel was simulated with the time-averaged mean scalar continuity equation for particles:

$$\bar{\boldsymbol{u}} \cdot \nabla c = (D_m + D_t)\nabla^2 \bar{c} - \frac{\partial}{\partial z} v_{se} \bar{c} \pm \sum_{n=1}^{c_{e,t}} \bar{R}_n \tag{7}$$

with c (# cm^{-3}), the particle concentration and $\boldsymbol{u}$ (m s^{-1}), the wind velocity in the x-, y- and z-direction. The particle concentration flux (left hand side of eqn. 7) equals, in order of appearance on the right hand side, the sum of: diffusion, gravitational settling, represented by the sedimentation velocity (v_{se}, m s^{-1}), and a reaction rate term, R_n, involving deposition and resuspension in this research (see section 2.2.3). Particle movement by diffusion included both molecular and turbulent diffusivity, represented by their coefficients D_m (m^2 s^{-1}) and D_t (m^2 s^{-1}), respectively. D_m was calculated with the slip-flow corrected Stokes-Einstein equation for spherical particles as follows:

$$D_{m,i} = \frac{k_B T}{3\pi\mu d_{p,i}} C_{c,i} \tag{8}$$

with k_B (1.380649·10^{-23} J K), the Boltzmann constant, T (K), the absolute temperature, μ (Pa s), the dynamic viscosity of air, d_p (m), aerodynamic diameter of the particle, and C_c (-), the Cunningham slip correction factor. The latter is given as: $C_c = 1 + 2\frac{\lambda_a}{d_{p,i}}(1.257 + 0.4e^{\frac{-1.1 \cdot d_{p,i}}{2 \cdot \lambda_a}})$. The particle turbulent diffusivity was calculated as:

$$D_t = \frac{\nu_t}{Sc_t} \tag{9}$$

with ν_t (m^2 s^{-1}), the turbulent kinematic viscosity and Sc_t (-), the turbulent Schmidt number, a measure for turbulent mixing. It was already acknowledged that the value of Sc_t is determining the accuracy of the concentration field profoundly and its value ranges between 0.3 - 1.5 depending on the configuration (Gromke and Blocken, 2015; Petroff et al, 2009). As this study does not aim to study the influence of Sc_t, the default value of 0.7 was adopted. Equation 7 was discretised using a finite element scheme with a quadratic truncation.

2.2.3 Particle deposition

The study entailed particles from ultrafine to coarse size range, so all PM deposition mechanisms by which PM can be deposited on the leaves of green wall species had to be included in the reaction term R_n of equation 7. The different mechanisms that play a role are sedimentation, Brownian diffusion, interception, inertial impaction, and turbulent impaction. The total deposition velocity, v_d, represents the superposition of all these mechanisms and corresponds to the deposition velocity calculated with the PM concentration and wind speed measurements (eqn. 3). The reaction term, R_n, is then expressed as:

$$\begin{aligned} R_n &= -LADv_dc \\ &= -LAD(v_{se} + v_{bd} + v_{in} + v_{im} + v_{ti})c \end{aligned} \tag{10}$$

with LAD (m^2 m^{-3}), the leaf area density, v_d (m s^{-1}), the total deposition velocity, c (# cm^{-3}), the particle concentration, v_{se} (m s^{-1}), sedimentation velocity, v_{bd} (m s^{-1}), Brownian diffusion velocity, v_{in} (m s^{-1}), interception velocity, v_{im} (m s^{-1}), impaction velocity, and v_{ti} (m s^{-1}), turbulent impaction velocity.

The different removal mechanisms were described by Zhang et al (2001) and Petroff and Zhang (2010), and their formulations were used in this research. They will be referred to in this article as the Zhang model and Petroff model, respectively. The formulation of the PM deposition mechanisms by each model is given in Table 3. The main difference between the two models is the use of the friction velocity, u_* ($= \sqrt{C_d U^2}$), in Zhang model, and the mean wind speed, U, in the Petroff model, to describe turbulence effects. Several studies have highlighted the importance of turbulence in the PM deposition process: Brownian diffusion deposition increased with the level of turbulence (Pryor et al, 2008). In addition, removal by interception and impaction will be enhanced in high turbulent flows, since particles will not be able to

follow the unsteady streamlines and will detach more easily from the streamlines to become deposited on leaf surfaces (Price et al, 2017). Hence, the different formulation of turbulence between the Zhang and Petroff model could be a first reason for different model outcomes. Second, the Zhang model includes particle resuspension subsequent to deposition (R in Table 3). Third, the models differ in the model constants used. Zhang uses one constant for all deposition mechanisms, namely θ, which is set equal to 3 independent of the land type. In contrast, the Petroff model includes a model constant for each deposition mechanism, namely C_{bd}, C_{in}, C_{im} and C_{ti} for deposition by Brownian motion, interception, impaction and turbulent impaction, respectively. These parameters depend on the land type and in this study the values were taken for a broadleaf canopy.

Deposition mechanism	Zhang model	Petroff model
Sedimentation	$v_{se} = \frac{C_c g \rho_p d_p^2}{18\mu}$	$v_{se} = \frac{C_c g \rho_p d_p^2}{18\mu}$
Brownian diffusion	$v_{bd} = \theta R Sc^{-\gamma} u_*$	$v_{bd} = C_{bd} Sc^{-\gamma} Re_l^{-1/2} U$
Interception	$v_{in} = \theta R \frac{1}{2} (\frac{d_p}{l})^2 u_*$	$v_{in} = C_{in} \frac{d_p}{l} [2 + ln \frac{4l}{d_p}] U$
Inertial impaction	$v_{im} = \theta R (\frac{St}{St+\alpha})^2 u_*$	$v_{im} = C_{im} (\frac{St}{St+\alpha})^2 U$
Turbulent impaction	N. c.	$v_{ti} = \begin{cases} 2.5 \cdot 10^{-3} C_{ti} \tau_p^{+2} u_* & \tau_p^{+2} < 20 \\ C_{ti} & \tau_p^{+2} u_* \geq 20 \end{cases}$

The symbols in order of appearance represent the following: C_c, the Cunningham slip-flow correction factor, g, the gravitational acceleration (9.81 m s^{-1}), ρ_p, the particle density (kg m^{-3}), d_p, the particle diameter (m), μ, the dynamic viscosity of air (Pa·s), θ, Zhang model constant (= 3), R, reduction in collection by rebound, Sc, Schmidt number, γ, Zhang (= 0.67) and Petroff (= 0.56) Brownian diffusion model constant for broadleaves, u_*, friction velocity (m s^{-1}), C_{bd}, Petroff Brownian diffusion model constant for broadleaves (1.262), Re_l, obstacle Reynolds number, U, average wind speed (m s^{-1}), l, characteristic obstacle length (m), C_{in}, Petroff interception model constant for broadleaves (0.216), St, Stokes number, α, Zhang (0.6) and Petroff (0.47) impaction model constant for broadleaves, C_{im}, Petroff inertial impaction model constant for broadleaves (0.13), C_{ti}, Petroff turbulent impaction model constant for broadleaves (0.056), τ_p^+, particle relaxation time. N.c. stands for not considered (i.e. no turbulent impaction in Zhang's model).

Table 3 The description of the deposition mechanisms by Zhang et al (2001) and Petroff and Zhang (2010).

2.2.4 Grid and boundary conditions

Each grid was composed of tetrahedral cells with a refined grid on the walls. Boundary layers were introduced with a thickness correction factor of 1.5. A grid convergence study was carried out for a wind tunnel parameterised for the effect of *H. helix* on airflow for the three Beaufort classes tested. Richardson interpolation was used to calculate the incoming mean wind speed (U_{in} on Figure 1). The grid convergence index (GCI) was calculated for the finest grid solution with a safety factor F_s equal to 3 for each Beaufort class. The results, shown in Table 9 (Appendix B), demonstrate that the results converged with increasing grid refinement. In addition, the normalised wind speed and turbulence intensity profiles at the four measurement locations (Front.z, Front.y, Back.z, Back.y) show fair agreement with the measured counterparts (Figure 3). However, deviations from the measured turbulence intensity were noted near the walls, probably related to a recirculation zone that was modelled, but not measured.

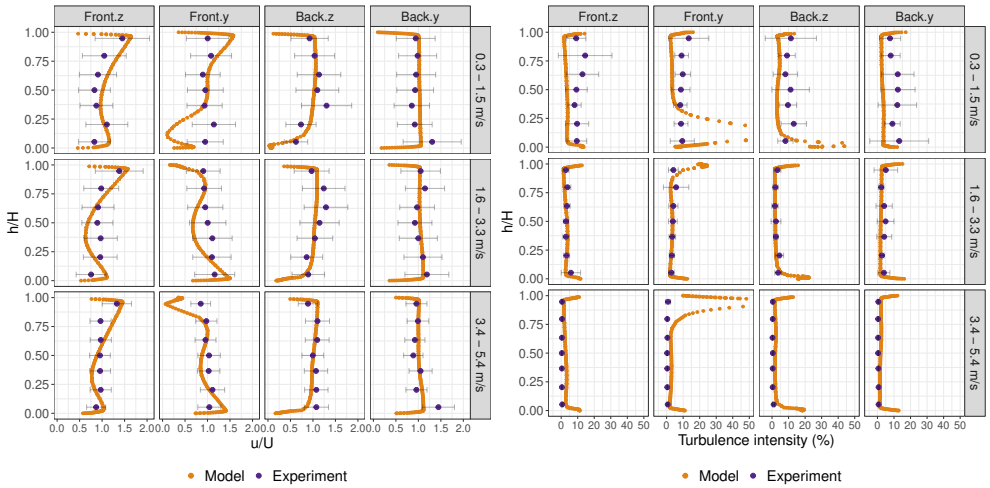

Fig. 3 Vertical profiles of normalised wind speed (left graph) and turbulence intensity (%, right graph) at the in- and outlet of the plant section (Figure 1 in both the y- and z-direction for modelled and measured data for the three Beaufort classes under study. The error bars represent the standard deviation on the measurements.

3 Results

3.1 Influential factors of collection efficiency

The LMM comparing the collection efficiency (*CE*) in a wind tunnel without and with *H. helix* showed significant differences among them ($p = 6.8 \cdot 10^{-5}$) with on average 13% higher values of *CE* for the case with *H. helix*. Therefore, the statistical analysis and validation was performed with the collected correction efficiency (CE_{cor}, %) of equation 2.

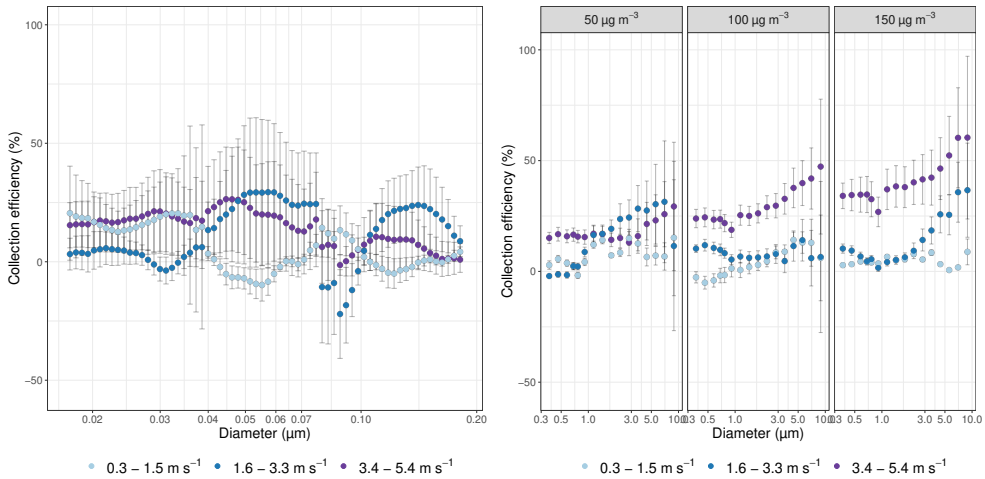

Fig. 4 Corrected collection efficiency (CE_{cor}, %) of particles consisting of soot with a particle diameter between 0.01 and 0.33 µm (left graph). For soot, particle diameters of each tested setting with the highest PM concentration of each tested setting of Table 2 were combined in one dataset of which CE_{cor} is shown here. In addition, CE_{cor} of particles consisting of dust with a particle diameter between 0.37 and 10 µm (right graph). The dust particles were generated in three PM_{10} concentrations, namely 50, 100 and 150 µg m^{-3}, shown on top of each graph (Table 2). CE_{cor} was determined for Beaufort classes 1 - 3 (Table 8). The x-axis is subjected to a logarithm transformation and the error bars represent the standard deviation of the measured values.

Figure 4 (left) shows the corrected collection efficiency of soot particles smaller than 0.3 µm. As already mentioned, in the case of soot, particle diameters with the highest PM concentration of each tested setting (Table 2) were combined in one dataset, so that only one CE_{cor} was obtained for each particle size and each Beaufort class. CE_{cor} did not seem to vary with particle diameter or wind speed. For particles > 0.04 µm,

the Beaufort class 'light breeze' (1.6 - 3.3 m s^{-1}) showed the highest CE_{cor}, while for the class 'light air' (0.3 - 1.5 m s^{-1}) negative values were observed. A negative value was seen when an empty wind tunnel removed approximately the same amounts of PM from the air stream as a wind tunnel with *H. helix*. For the two highest Beaufort classes a minimum CE_{cor} was observed for a particle diameter between 0.079 and 0.1 µm. Figure 4 (right) shows the measured CE_{cor} for particles of the fraction $PM_{2.5}$ and PM_{10}, thus consisting of dust. Three different PM_{10} concentrations were tested across three successive Beaufort scales. All these conditions were summarised in Table 2 and Table 8 (Appendix A), respectively. It was witnessed that for a given incoming particle concentration, CE_{cor} increased with increasing particle diameter, however it was accompanied by higher standard deviations. This is related to the fact that the highest particle diameters are low in number concentrations, so concentration differences were magnified. For Beaufort classes 1 to 3, CE_{cor} for PM_{10} was on average for all concentrations, 3 ± 5, 12 ± 9 and 14 ± 3% higher than $PM_{2.5}$, respectively. In addition, deposition was amplified with increasing wind speed. Compared with the lowest Beaufort class 'light air' (0.3 - 1.5 m s^{-1}), on average for all concentrations, CE_{cor} of $PM_{2.5}$ was 2 ± 2 and 21 ± 4 % higher for the class 'light breeze' (1.6 - 3.3 m s^{-1}) and 'gentle breeze' (3.4 - 5.5 m s^{-1}), respectively.

The output of the LMM showed that corrected collection efficiency of *H. helix* increased significantly with particle diameter and wind speed, but did not depend on RH and the particle source (Table 4). However, significant interactions existed between particle source and diameter, and particle source and wind speed, visualised in Figure 5. It demonstrated that with increasing particle diameter, CE_{cor} decreased for particles with $d_p < 0.3$ µm, while it increased for $d_p > 0.3$ µm (Figure 5, left). Furthermore, wind speed had a more pronounced positive effect on CE_{cor} of dust particles compared with soot particles (Figure 5, right).

Table 4 Results of the LMM analysis relating the corrected collection efficiency, CE_{cor} % to particle diameter (µm), incoming wind speed (m s^{-1}), relative humidity (RH, %) and PM source and the interactions among them (denoted with 'x'), in terms of the F and p value.

Effect	F value	p value
Diameter	7.313	$6.975{\cdot}10^{-3}$
Wind speed	15.537	$2.412{\cdot}10^{-4}$
RH	1.877	0.177
PM_{source}	0.092	0.762
Diameter x PM_{source}	54.448	$3.584{\cdot}10^{-13}$
U_{in} x PM_{source}	81.206	$<2.2{\cdot}10^{-16}$

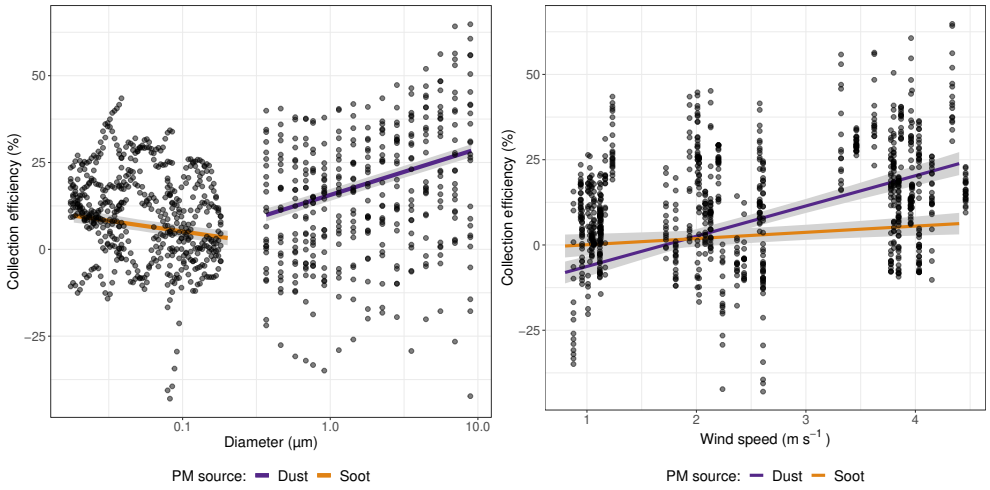

Fig. 5 Visualisation of the significant interactions determining the corrected collection efficiency (CE_{cor}, %) in the LMM model (Table 4). The graphs include the interaction between particle diameter (µm) and particle source (PM_{source}, i.e. dust or soot) (left graph), and between wind speed (U_{in} (m s^{-1})) with particle source (PM_{source}, i.e. dust or soot) (right graph). Points in black show measured values of CE_{cor} as a function of wind speed.

3.2 Model validation

Figure 6 (left) shows the measured corrected collection efficiency and the modelled collection efficiency, both referred to as CE, for the Zhang and Petroff model with the results for PM consisting of soot. For soot, it was observed that the Zhang model showed better agreement with the measured values (root mean square error (RMSE) $< 7\%$ across all Beaufort classes, indicated by $RMSE_z$) in comparison with Petroff's

model (RMSE $< 14\%$ across all Beaufort classes, indicated by RMSE_p). The main mechanism was Brownian diffusion, accounting for 99.9% of the total deposition velocity (Figure 6, right). Therefore, the other deposition mechanisms are not visible on this graph. Brownian diffusion was also the main deposition mechanism in Petroff's model, however their Brownian deposition velocity was at least two orders of magnitude smaller for a particular particle diameter compared with the one from Zhang's model, which resulted from the negative root of the obstacle Reynolds number ($Re_l^{-1/2}$ in Table 3). The obtained RMSE values were therefore on average 3 times higher compared with Zhang's model. Zhang's model showed a higher deviation from the measurements at the highest wind speed. It could indicate that the use of the friction velocity, u_*, caused deviations at larger wind speeds. This may be due to the fact that the friction velocity in Zhang's model is a parameter to describe drag at the top of the canopy and not within plant packages (Zhang et al, 2001). However, the influence of drag was already parameterised in the airflow model, and working with $u_* = \sqrt{C_d U^2}$ consequently accounted for this effect twice. Wind speed had a minimal effect on *CE* obtained with the Zhang model, in line with was found for the experimental data (Figure 5, B). However, wind speed had a more pronounced effect on the deposition velocity (seen by the increasing y-axis of Figure 6, right) and this makes sense since v_d is the product of flow rate and *CE*. These findings were in line with other authors (Beckett et al, 2000; Freer-Smith et al, 2004).

For soot particles with $d_p > 0.3$ µm, Zhang's model calculated too low collection efficiencies for all particle sizes. Fair agreement of Petroff's model was observed for the lowest wind speed ($\text{RMSE}_p < 12\%$), but for the higher wind speeds deviations were more pronounced ($\text{RMSE}_p \sim 30\%$). Although, from a certain particle size, depending on the wind speed class, model results fell within the standard deviation of the measured values. More specifically, there was better agreement for 1.6 - 3.3 m s^{-1} above 3

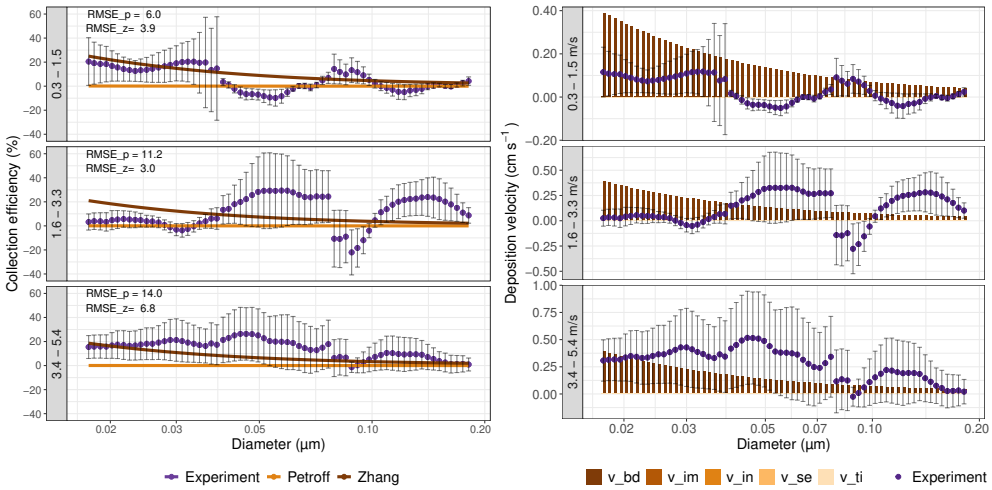

Fig. 6 Measured ('Experiment') and modelled ('Petroff' and 'Zhang') collection efficiency (%) of soot particles (0.02 - 0.20 µm) for Beaufort classes 1 - 3 (left graph). Measured total v_d (cm s^{-1}, purple bullets) and modelled v_d (m s^{-1}, bar plot) of each PM deposition mechanisms (right graph). The 1^{st} bar represents the Petroff model and the 2^{nd} bar the Zhang model. The bars of Zhang's model are not visible, since their value was very low compared to Petroff's model. The x-axis is subjected to a logarithm transformation and the error bars represent the standard deviation of the measured values.

µm and for 3.4 - 5.5 m s^{-1} above 2 µm. This increase in *CE* of the Petroff model corresponded with the occurrence of turbulent impaction, which became at those particle diameters the main deposition mechanism with a relative contribution to the total deposition velocity of 91 and 83% for Beaufort class 2 and 3, respectively (Figure 7, right). However, turbulent impaction reached a constant value with increasing particle diameter, which was not seen in the measurements. The second important deposition mechanism was sedimentation at Beaufort class 1 (5%) and 2 (3%) and both interception and impaction at Beaufort class 3 (both ∼1.6%). Before the point at which turbulent impaction became important, the Petroff model showed the greatest removal by Brownian diffusion, but the total deposition velocity did not approach the measurements. The Zhang model showed a dominance of Brownian diffusion below ∼3 µm and at larger particle diameters deposition by sedimentation and impaction became prevalent at Beaufort class 1 and impaction alone at the higher wind speed classes. Particle rebound in Zhang's model was responsible for lowering Brownian diffusion,

interception and inertial impaction of d_p = 10 µm by 14, 18 and 23% for Beaufort classes 1, 2 and 3, respectively. In conclusion, both models failed to calculate the measured *CE* (v_d) values below ∼1.5 µm above 1.6 m s^{-1}. Above that particle diameter, the Petroff model approximated the measurements due to the inclusion of turbulent impaction. Within Beaufort class 3, RMSE increased with the incoming PM_{10} concentration. It could be that *H. helix* acted as a barrier that caused a blocking of the airflow, so that higher concentrations would be present in front of it (Abhijith et al, 2017; Pappa et al, 2023). However, in this study, the PM_{10} concentrations were set at the start of each experiment and higher concentrations due to blockage would already be accounted for. An optimised deposition model will be discussed in the next section.

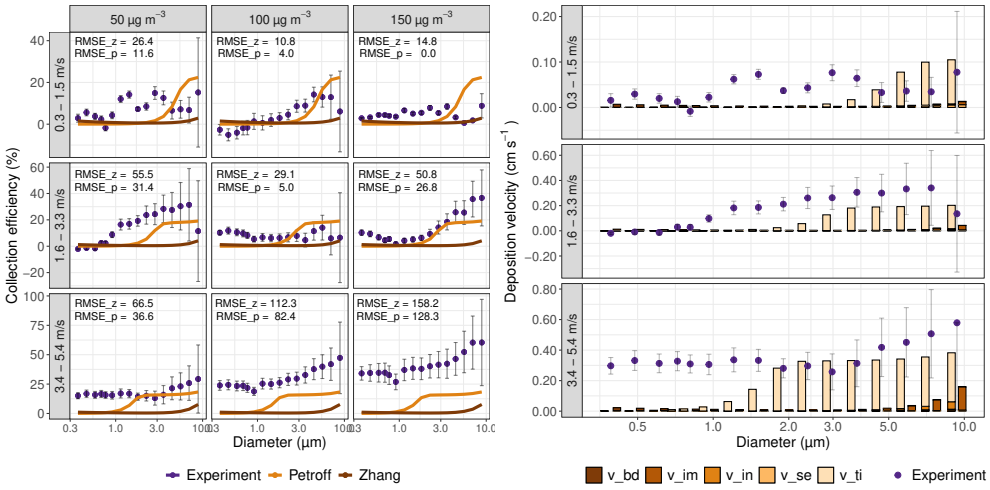

Fig. 7 Measured ('Experiment') and modelled ('Petroff' and 'Zhang') collection efficiency (%) of dust particles (0.37 - 10 µm) for the studied cases of Table 2 and for Beaufort classes 1-3 (left graph). Measured total v_d (m s^{-1}, bullets) and modelled deposition velocity (m s^{-1}, bar plot) of each PM deposition mechanisms (right graph) (1^{st} bar = Petroff model, 2^{nd} bar = Zhang model) for an incoming PM_{10} concentration of 50 µg m^{-3} (graphs of 100 and 150 µg m^{-3} are on Figure 11 (Appendix C)).

3.3 Model optimisation

To achieve an optimised PM deposition model ranging from ultrafine to coarse PM, the following issues needed to be improved: 1) deposition by Brownian diffusion should

not depend on the obstacle Reynolds number, 2) the influence of wind speed should not be parameterised in the deposition model since it is already inclduded in the air flow model, 3) deposition of particles between 0.3 - 2 µm should be enhanced at higher wind speeds, and 4) the deposition velocity should keep on increasing with particle diameter for $d_p > 3$ µm.

To address these discrepancies compared with the measured v_d, first a combination of the model of Zhang and Petroff is proposed. From the model of Zhang, the description of Brownian diffusion was employed, since it was able to approximate the measured v_d, while Petroff's description resulted in v_d values that were two orders of magnitude too small. However, the friction velocity was replaced with the mean wind speed, because drag was already parameterised in the air flow model. Turbulent impaction proved necessary to approximate the rise with particle size. Impaction became the dominant deposition mechanism in Zhang's model for $d_p > 2.8$ µm and their parametrisation could lead to a better agreement with the measurements with increasing particle diameter. On the other hand, Petroff's formulation of interception was specific for broadleaves, while Zhang was solely for needle leaves. Since little is known about the parametrisation of particle rebound, it was not included in the modified model. To conclude, Brownian diffusion and impaction were modelled with the definition of Zhang, while Petroff's description of interception and turbulent impaction was used, without the inclusion of the model constants C_{in} and C_{ti} of Table 3, since these are constants for whole canopies and they were also discarded in other studies (Petroff et al, 2009; Šíp and Beneš, 2017). At the lowest wind speed, the modified model exhibited a comparable performance to Zhang's model for soot particles (as depicted in Figure 8, left) and to Petroff's model for dust particles, which is remarked by the comparable RMSE (termed RMSE_{mod1}). However, as the wind speed increased, the modified model demonstrated better agreement with the measurements compared to both Zhang and Petroff models. For soot particles, RMSE_{mod1} was 2.4% and 4.5%

lower at Beaufort scale 2 and 3, respectively, in comparison to the Zhang model, which was considered the reference for soot due to Petroff's model showing more significant deviations from the measurements. Similarly, for dust particles, RMSE_{mod1} was approximately 47% and 46% lower at Beaufort scale 2 and 3, respectively, when contrasted with the Petroff model (8, right). In this case, the Petroff model was taken as the reference for dust because the Zhang model exhibited more pronounced discrepancies from the measurement data. The breakdown of the total deposition velocity in the different deposition mechanisms is shown on Figure 12 (Appendix C). The main discrepancy remained that *CE* was still underestimated for d_p = 0.3 - 2 µm. The modified model also provided a lower RMSE for PM from soot at wind speeds above 1.6 m s^{-1}, but a higher RMSE at the lowest wind speed.

Another way to improve the deposition model could be to include the effect of turbulence, since research has demonstrated that including the effects of free-stream turbulence resulted in an increase in deposition by impaction with one order of magnitude (Moran et al, 2013; Price et al, 2017). Therefore, these authors proposed a turbulent Stokes number to include the interaction of particles with turbulent eddies by combining the classical Stokes number (St) with the Taylor microscale Reynolds number (Re_λ) following:

$$St^* = St \cdot Re_\lambda^{0.3} \tag{11}$$

$$Re_\lambda = \frac{u'\lambda}{\nu} \tag{12}$$

with u' (m s^{-1}), the root-mean-square of the velocity perturbations, λ (m), the Taylor microscale, and ν (m^2 s^{-1}), the kinematic viscosity. λ describes the average distance at which the turbulent fluctuations (u') vary over two standard deviations in magnitude.

Price et al (2017) reported that *CE* on grass increased of 40% for particles with d_p = 8 µm at 3.8 m s^{-1} and this was accompanied by $Re_\lambda = 110$ and $\lambda = 0.009$ m. In this study, Re_λ amounted at the inlet of the test section to around 40, which was said to be the limit value below which turbulence is considered negligible (Moran et al, 2013). The modified model resulted in higher deposition velocities than measured (Figure 9, left) and it can be concluded that for low wind speeds it is not advised to include a turbulent Stokes number. The breakdown of the total deposition velocity in the different deposition mechanisms is shown on Figure 13 (Appendix C).

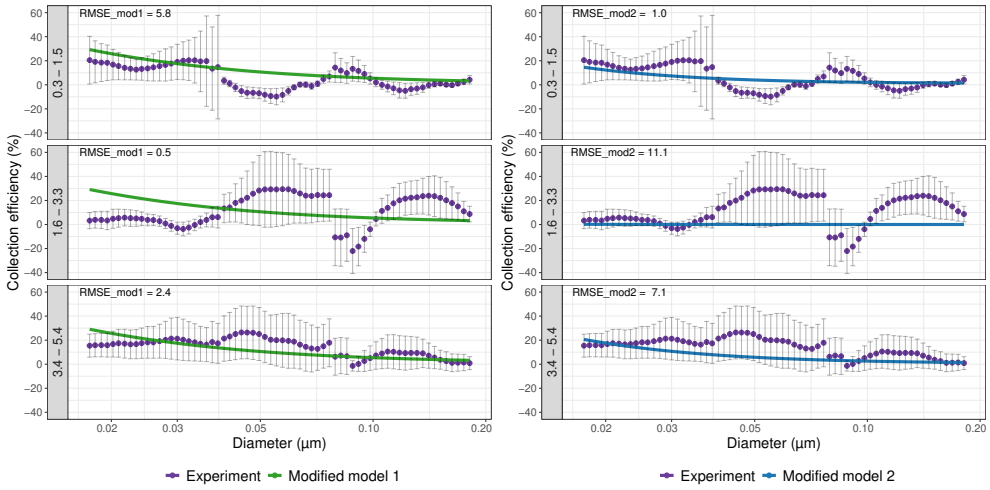

Fig. 8 Measured ('Experiment') and modelled corrected collection efficiency (%) of soot particles (0.02 - 0.20 µm) for the studied cases of Table 2 and for Beaufort classes 1 - 3 with on the left: modified model combining Zhang and Petroff, and on the right: modified model 2 with turbulent Stokes number.

3.4 Overall model validation

In the previous sections, RMSE was calculated to investigate the deviation of the modelled relative to the measured *CE* and v_d. Here, a validation is presented that includes all treatments in terms of wind speed, PM concentration and particle diameter, for the model of Zhang, Petroff and the modified model using a combination of Petroff and

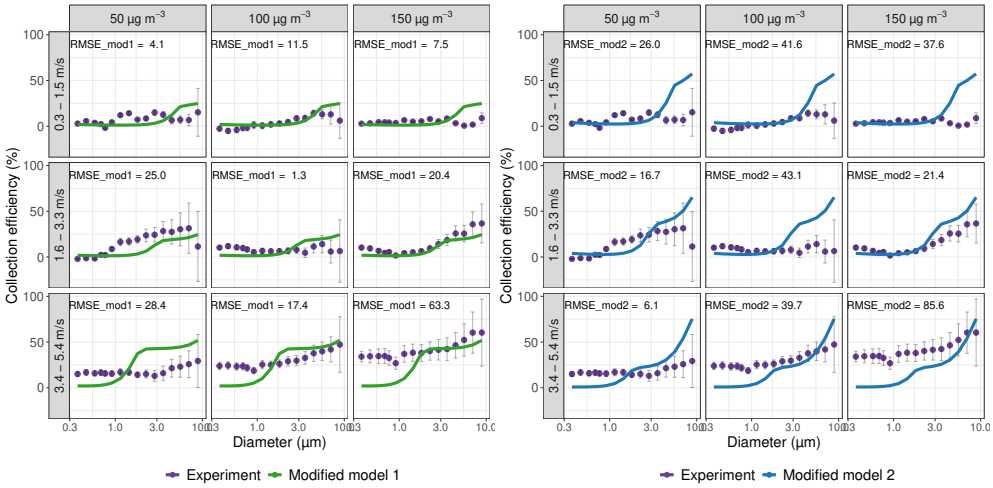

Fig. 9 Measured ('Experiment') and modelled corrected collection efficiency (%) of dust particles (0.37 - 10 µm) for the studied cases of Table 2 and for Beaufort classes 1 - 3 with on the left: modified model combining Zhang and Petroff, and on the right: modified model 2 with turbulent Stokes number.

Zhang. The adjusted model incorporating a turbulent Stokes number has not been considered in this context, as it was concluded that it did not yield better outcomes.

The performance metrics are presented in Table 5, revealing that all three models exhibit an underestimation of the measured CE and consequently v_d. This is evident from the positive fractional bias (FB) and the linear regression line below the identity line in Figure 10. Comparatively, the modified model demonstrates superior predictive accuracy characterised by a lower RMSE, reduced bias (lower FB), decreased scatter (higher fraction of modelled results within a factor two of the measurements (FAC2)), and less deviation from the measurements (normalised mean square error (NMSE)). In addition, the modified model had an overall better fit to the data (higher R-squared (R^2)), as opposed to the Zhang and Petroff model. This observation is further supported by Figure 10, which clearly illustrates how the linear regression line of the modified model approaches the identity line more closely when compared to the standard models. Assessing these metrics against the acceptance criteria defined by (Chang and Hanna, 2004), it is evident that the modified model satisfies the conditions for NMSE, while the model of Zhang and Petroff are not. The modified model

also meets the criterion for FB. Interestingly, this is also the case for the Zhang model. The criterion for FAC2 (> 0.5) was not met by any of the models.

Table 5 Root mean square error (RMSE), normalised mean square error, NMSE, fractional bias, FB, and fraction of modelled results within a factor two of the measurements, FAC2 for CE and v_d obtained with the model of Zhang, Petroff and a modified model for all runs. In addition, the R^2 is given.

Model	RMSE		NMSE		FB		FAC2	R^2
	CE (%)	v_d (cm s^{-1})	CE (%)	v_d (cm s^{-1})	CE	v_d		
Zhang	134.37	2.42	3.57	5.85	0.20	0.26	0.20	0.23
Petroff	179.99	2.81	6.13	7.73	0.31	0.33	0.08	0.31
Modified	3.55	0.36	0.94	1.02	0.004	0.03	0.37	0.57

Acceptance criteria are defined as: NMSE < 1.5, $-0.3 <$ FB < 0.3 and FAC2 > 0.5 (Chang and Hanna, 2004).

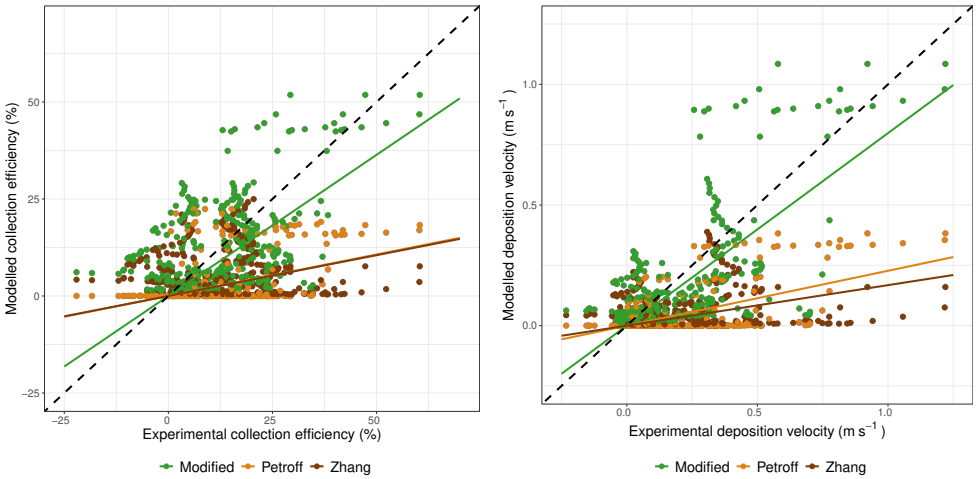

Fig. 10 Measured vs modelled corrected collection efficiency (%) (left graph) and deposition velocity (cm s^{-1}) (right graph) of all particles sizes, PM concentrations and Beaufort classes for the model of Zhang, Petroff and modified model combining Zhang and Petroff deposition models.

4 Discussion

4.1 Wind tunnel comparison

This study was among the few that determined the collection efficiency (CE) and deposition velocity (v_d) of PM representing urban pollution for particles from 0.02 up

to 10 µm. To compare our results with the literature, *CE* and v_d for $PM_{0.1}$, $PM_{2.5}$ and PM_{10} were calculated and shown in Table 6.

CE (and v_d) of $PM_{2.5}$ were reported for shoots packed in a test volume of a wind tunnel with oil droplets as $PM_{2.5}$ source at 1 m s^{-1} and were higher than what was found in the present study, namely ∼45 - 58% (3.9 - 11.1 cm s^{-1}) for broadleaved species with a LAD of 16 m^2 m^{-3} and 22 - 30 % (1.3 - 2.1 cm s^{-1}) for conifers with a LAD of 26 m^2 m^{-3} (Shen et al, 2022). On the other hand, much lower *CE* and v_d were found with wind tunnel studies using NaCl particles with a mean diameter of 0.8 ± 0.2 - 1.28 ± 0.07 µm on shoots of small trees: at an approaching wind speed of 1 m s^{-1}, 0.03 ± 0.02% (0.03 ± 0.03 cm s^{-1}) for broadleaves and 0.21 ± 0.03 % (0.11 ± 0.02 cm s^{-1}), and at an approaching wind speed of 3 m s^{-1}, 0.07 ± 0.06% (0.2 ± 0.6 cm s^{-1}) for broadleaves and 0.32 ± 0.06% (1.0 ± 0.2 cm s^{-1}) (Beckett et al, 2000; Freer-Smith et al, 2005). The found deposition velocity of our study was in line with values reported for uranium particles of 0.82 µm size for a wind speed of 0.52 m s^{-1} within a spruce canopy, namely 0.6 ± 1.6 cm s^{-1} in this study and 0.515 cm s^{-1} in the study of Ould-Dada (2002). In the case of $PM_{0.1}$, *CE* were similar (Huang et al, 2013) or lower (Wang et al, 2019) than reported in the literature. The first study was on wind tunnel experiments with soot from burning candles, obtained *CE* of roughly 10% by *Juniperus chinesis* (coniferous evergreen, LAD of ∼200 m^2m^{-3}) packages at wind speeds below 1 m s^{-1} (Huang et al, 2013). In the second study, shoots of different broadleaf and needle leaf tree species were subjected to an airflow of 1 m s^{-1} containing diesel exhaust for which *CE* values of ∼30 - 80% were reported (Wang et al, 2019). Overall, the comparison between studies is complex since particle size, wind speed and plant species are all influencing PM deposition. It can be remarked, however, that the present study looked at a climber presented in its natural form (no packages) and with a more realistic LAD (12.3 ± 0.1 m^2 m^{-3}), justifying the lower *CE* and v_d values of this study compared with the literature. In addition, *H. helix* was attributed as a low

PM scavenger based on PM measurements on leaf surfaces due to unfavourable leaf traits regarding PM deposition (Muhammad et al, 2019; Weerakkody et al, 2017).

This study demonstrated that PM deposition is related to particle size and wind speed, but relative humidity and the type of soot did not have an impact. For particles with $d_p < 0.2$ µm, *CE* was inversely proportional with particle size, while wind speed had a small positive impact. For particles with $d_p > 0.3$ µm, *CE* was proportional with particle size and wind speed. A minimum particle deposition was found between ∼0.08 - 0.1 and between ∼0.2 - 2 µm. The latter coincides with the model of Zhang, which has no efficient particle deposition mechanism around 1 - 2 µm. Other studies confirmed that *CE* (v_d) increased remarkably with wind speed, since in high turbulent flows deposition by Brownian diffusion, interception and impaction are enhanced (Beckett et al, 2000; Freer-Smith et al, 2004; Price et al, 2017). The effect of humidity did not play a role in particle deposition for the wind tunnel experiments of this study. Hygroscopic growth was not likely to take place for the generated PM here, since hygroscopic growth is only considerable for particles containing water-soluble compounds such as ammonium sulphate or salt (Katata et al, 2014; Zhang et al, 2001). Furthermore, coagulation was unlikely to occur during the short particle residence time in the test section of the wind tunnel (Steffens et al, 2012). Therefore, it was justified that hygroscopic growth and coagulation were not included in the deposition model.

Table 6 Measured collection efficiency (*CE*, %) and deposition velocity (v_d, m s^{-1}) for the fraction $PM_{0.1}$, $PM_{2.5}$ and PM_{10} for the three investigated Beaufort classes.

Beaufort	Wind speed (m s^{-1})	Fraction	*CE* (%)	v_d (cm s^{-1})
1	0.3-1.5	$PM_{0.1}$	12.0 ± 0.1	0.070 ± 0.009
1	0.3-1.5	$PM_{2.5}$	-0.08 ± 1.6	0.004 ± 0.01
1	0.3-1.5	PM_{10}	4 ± 11	0.04 ± 0.05
2	1.6-3.3	$PM_{0.1}$	1.26 ± 0.015	0.002 ± 0.001
2	1.6-3.3	$PM_{2.5}$	8 ± 2	0.2 ± 0.3
2	1.6-3.3	PM_{10}	22 ± 21	0.04 ± 0.03
3	3.4-5.5	$PM_{0.1}$	18.0 ± 0.2	0.36 ± 0.01
3	3.4-5.5	$PM_{2.5}$	13 ± 4	0.48 ± 0.09
3	3.4-5.5	PM_{10}	23 ± 18	0.8 ± 0.3

4.2 Deposition model

In this study, the numerical modelling of dry deposition on a climber was reported based on the often cited canopy deposition models of Zhang (Zhang et al, 2001) and Petroff (Petroff and Zhang, 2010). Fair agreement of the Zhang deposition model with wind tunnel experiments was observed for particles smaller than 0.18 µm (RMSE < 13%). Steffens et al (2012) suggested that for particles smaller than 0.1 µm the model of Zhang performed better than Petroff's model, however they both deviated from measurements for particles < 0.05 µm behind a vegetation barrier. The models did show an overestimation of the simulated wind speed behind the barrier, so that the use of the friction velocity of Zhang's model, including vegetation drag, improved the modelling of v_d. However, in the present study, the influence of vegetation on the air flow was already incorporated in the air flow model, and the use of the friction velocity caused more deviations from the measurements. Therefore, separate validation of the flow field and concentration pattern assured that model errors did not propagate. This is an often seen problem in state-of-the art deposition models that lack validation data. For particles with $d_p > 0.3$ µm, the model of Petroff showed fair agreement at a wind speed of 1 m s^{-1}, but showed underestimations at higher wind speeds. Amicarelli et al (2021) used the model of Petroff to model deposition of particles of 0.82 µm to a scaled spruce forest at a wind speed of 0.52 m s^{-1} (Ould-Dada, 2002). The experimental deposition velocity averaged over the canopy depth was underestimated by 24% by the model. This underestimation is consistent with this study, which showed that the model underestimated the measurements for particle sizes between 0.3 - 2 µm. For 0.82 µm, interception and inertial impaction accounted for 87% and 9% of the total deposition velocity, respectively (Amicarelli et al, 2021), since they did not include Brownian diffusion. However, a larger Brownian collection efficiency is assigned to broadleaves (Petroff and Zhang, 2010).

To overcome the discrepancies between measured and modelled *CE* (v_d), a new dry deposition model was proposed including the best features of Zhang's and Petroff's model which were seen as the reference model for $PM_{0.1}$ and for $PM_{2.5}$ and PM_{10}, respectively. The modified model exhibited a comparable RMSE at the lowest wind speeds, but at the highest wind speeds it approached the measurements much better with a reduction of the RMSE of approximately 2.4% and 4.5% at Beaufort scale 2 and 3, respectively, in comparison to the Zhang model for soot. Similarly, for dust particles, the RMSE of the modified model was approximately 47% and 46% lower at Beaufort scale 2 and 3, respectively, when contrasted with the Petroff model. Taking all particle sizes, concentrations and wind speeds into account, the modified model was able to meet the following acceptance criteria for air quality models (Chang and Hanna, 2004): NMSE = 0.94 for *CE* (1.76 for v_d) < 1.5, -0.3 < FB = 0.004 for *CE* (0.03 for for v_d) < 0.3. The criterion of FAC2 > 0.5 was not satisfied by the modified model. In addition, the R^2 was increased from 0.23 (Zhang's model) and 0.31 (Petroff's model) to 0.57 (modified model). The modified model with an enhancement of deposition with turbulence was not in accordance with the measurements and this was probably due to the low wind speeds in this study. Deposition models for $PM_{0.1}$ to tree species were characterised by a RMSE of 5 to 15%, depending on the tree species and the wind speed (Huang et al, 2015), and by a RMSE of 9 to 18% and a R^2 of 0.32 up to 0.93, depending on tree species and the amount of plant material (Lin et al, 2012). Therefore, modified model was highly competitive compared to deposition models reported in the literature. Moreover, it considered the complete PM size range.

5 Conclusions

Dry deposition of particles is an important process determining PM concentrations and the modelling of this process is regarded an important aspect in air quality modelling. This study presented an update of the models described by Zhang et al (2001) and

Petroff et al (2009) using validation data for the complete PM size range relevant for human health. Overall, the modified model was able to simulate dry deposition with a RMSE of 3.55% for CE and 0.36 cm s^{-1} for v_d. The model is, therefore, highly competitive against previously described models and can be used to model PM deposition on plant species, provided the correct parameterisation of the drag by this species.

As a result, the model can be used to map the impact of green walls and, by extension other types of UGI, on air quality in cities and thus respond to the need for more healthy living environments in cities. Notwithstanding, to fully validate the proposed model, PM deposition experiments with different plant species should be conducted and the model still showed an underestimation for particle sizes of 0.3 - 2 µm at higher wind speeds. Discrepancies between measured and modelled deposition velocities are explained in the literature by an incorrect description of the vertical variation in leaf area density (LAD). It is seen for climbers that the amount of leaves, and thus their LAD, decreases with height (Pérez et al, 2017). In this study a uniform coverage of *H. helix* was foreseen, but some parts along the screen were probably more covered than others and leaf overlapping was present. Areas with a higher concentration of leaves may exhibit lower PM deposition, which is currently not included on the model. Determination of the spatial variability of LAD could improve the model results.

It should be emphasised that the measured CE cannot be directly extrapolated to draw conclusions about the CE of an actual green wall. This limitation arises because the wind tunnel setup did not include the wall behind the green wall. When the wind is perpendicular to the wall, it can cause the airflow to deflect, leading to air passing parallel to the green wall. This intricate flow pattern is challenging to replicate accurately in a wind tunnel setup, rendering it a complex phenomenon to study. To validate a dry deposition model, a perpendicular orientation relative to the airflow was selected as the ideal scenario, as it offered the highest expected reduction in PM

concentrations. Nevertheless the obtained model is applicable to study PM deposition in the case of other wind directions relative to the vegetation or in the case a wall is present. This is so because the drag parameters are intrinsic, and changes in wind flow are accounted for within the air flow model. The wind speed dependent drag parameters play a crucial role in ensuring that the model incorporates the deceleration of wind speed within the vegetation. This modeling approach extends to the dispersion and deposition of PM, effectively accounting for this effect.

Uncertainties emerge from the wind tunnel setup due to PM measurement uncertainties, precarious stable PM concentrations at the inlet of the test section, and possible unsteady flow in the test section. Additionally, variations in outdoor PM concentrations were of significance. For $PM_{0.1}$, these variations had minimal impact, as the generated $PM_{0.1}$ led to concentrations within the wind tunnel that were 10 to 100 times higher than the outdoor concentration. Conversely, $PM_{2.5}$ and PM_{10} levels fluctuated during the day. To minimise this effect, experiments were consistently conducted during a specific time period, from 10 am to 5 pm, each day. Furthermore, temperature and relative humidity naturally fluctuate throughout the day and across seasons. Consequently, the meteorological conditions were not consistent for every experiment. However, efforts were made to mitigate this variability by incorporating outdoor condition measurements into the statistical analysis. Moreover, measurements were done along the transect of the in- and outlet of the test section to average differences in wind speed and PM concentration along these transects. A closed-circuit wind tunnel would allow to perform experiments under more controlled conditions. Moreover, more advanced wind tunnels exist that include complete scaled-down urban geometries. It would be of interest to study in atmospheric boundary layer wind tunnel setups PM deposition on real vegetation with PM consisting of a composition that is found outdoors. This would broaden the scope of the experiments from parameter estimation and model optimisation towards case studies in a complex urban environment.

Declarations

Funding

T.Y. is supported as doctoral candidate (Strategic basic research) from the Research Foundation - Flanders (FWO, 1S88919N). The paticulate matter measurement and generating devices were obtained through a basic research infrastructure grant of the University of Antwerp (Belgium). The data from the weather station were provided by Taher Ghalandari from the Energy and Materials in Infrastructure and Buildings (EMIB) group at the University of Antwerp (Belgium).

Competing interests

The authors declare that they have no known competing financial interests or personal relationships that could have appeared to influence the work reported in this paper.

Author's contributions

All authors contributed to the study conception and design. Material preparation, data collection, data analysis, and model construction and validation were performed by Tess Ysebaert. The first draft of the manuscript was written by Tess Ysebaert and all authors commented on previous versions of the manuscript. All authors read and approved the final manuscript.

Ethics approval

Not applicable.

Consent to participate

Not applicable.

Consent for publication

Not applicable.

Data availability

The particulate matter concentration and wind speed measurements generated during the current study are available in the Zenodo repository (https://doi.org/10.5281/zenodo.7771857).

Code availability

Not applicable.

Abbreviations

C_d sectional drag coefficient

LAD leaf area density

Re Reynolds number

CFD computational fluid dynamics

TKE turbulent kinetic energy

SDR specific dissipation rate

sRANS Steady Reynolds-averaged Navier-Stokes

U_{bulk} bulk mean wind speed

LA leaf area

K permeability

DE (spatial) discretisation error

GCI grid convergence index

LMM linear mixed model

CE collection efficiency

CE_{cor} corrected collection efficiency

$C_{in,cor}$ corrected incoming PM concentration

v_d deposition velocity

PMparticulate matter

$PM_{0.1}$ ultrafine PM

$PM_{2.5}$ fine PM

PM_{10} coarse PM

UFP ultrafine particles

RH relative humidity

T temperature

PSD particle size distribution

SMPS scanning mobility particle sizer

OPS optical particle sizer

UGI Urban green infrastructure

WHO World Health Organisation

RMSE root mean square error

NMSE normalised mean square error

FB fractional bias

R^2 R-squared

FAC2 fraction of modelled results within a factor two of the measurements

A Conditions of the incoming air stream

The table below provides the meteorological conditions of the incoming air stream measured at the inlet of the plant section, for an empty wind tunnel system (i.e. blanco) and for a wind tunnel with Hedera helix.

Table 7 The wind speed, U_{in} (m s^{-1}), relative humidity, RH (%), and temperature, T (°C), of the incoming air stream, measured at the inlet of the plant section, for an empty wind tunnel system (i.e. blanco).

Beaufort	Test	U_{in} (m s^{-1})	RH (%)	T (°C)
1	a	1.3 ± 0.2	77 ± 3	20.1 ± 0.2
2	a	2.3 ± 0.2	70 ± 1	19.90 ± 0.04
3	a	3.84 ± 0.08	79 ± 1	13.7 ± 0.4
1	b	1.3 ± 0.1	81.3 ± 0.9	15.5 ± 0.2
2	b	2.3 ± 0.1	78.7 ± 0.8	15.91 ± 0.03
3	b	3.72 ± 0.09	89.7 ± 0.5	12.3 ± 0.6
1	c	1.0 ± 0.2	80 ± 3	16.6 ± 0.2
2	c	2.3 ± 0.1	74 ± 1	10.8 ± 0.1
3	c	3.93 ± 0.09	72 ± 2	15.9 ± 0.2

Table 8 The wind speed, U_{in} (m s^{-1}), relative humidity, RH (%), and temperature, T (°C), of the incoming air stream, measured at the inlet of the plant section, for a wind tunnel system with *H. helix*. The associated permeability, K (m^2), and drag coefficient, C_d (-), calculated with previously determined relations for *H. helix* with a LAD of 13.307±0.007 m^2m^{-3} (Ysebaert et al, 2022), are also given.

Beaufort	Test	U_{in} (m s^{-1})	RH (%)	T (°C)	K (m^2)	C_d (-)
1	a	1.3 ± 0.1	66 ± 26	17.1 ± 0.3	$1.814 \cdot 10^{-5}$	0.62
2	a	2.3 ± 0.2	87 ± 37	12.1 ± 0.3	$1.814 \cdot 10^{-5}$	0.47
3	a	4.0 ± 0.1	69 ± 28	16.0 ± 0.3	$1.814 \cdot 10^{-5}$	0.36
1	b	1.1 ± 0.1	68 ± 27	16.6 ± 0.2	$1.765 \cdot 10^{-5}$	0.68
2	b	2.2 ± 0.5	66 ± 32	14.8 ± 0.2	$1.814 \cdot 10^{-5}$	0.45
3	b	3.93 ± 0.08	58 ± 23	20.0 ± 0.3	$1.814 \cdot 10^{-5}$	0.36
1	c	1.1 ± 0.2	72 ± 26	18.4 ± 0.6	$1.784 \cdot 10^{-5}$	0.68
2	c	2.4 ± 0.3	84 ± 25	11.02 ± 0.03	$1.814 \cdot 10^{-5}$	0.48
3	c	3.9 ± 0.09	74 ± 28	18.3 ± 0.5	$1.814 \cdot 10^{-5}$	0.36

B Grid convergence study

The table below shows the results of the grid convergence study of the present study.

Table 9 Outcome of a grid convergence study of the incoming mean wind speed (U_{in}) for Beaufort classes 1 to 3, in terms of (spatial) discretisation error (DE) (%) and GCI (%) relative to the finest grid.

Beaufort number	Number of cells	Wind speed (m s^{-1})	DE (%)	GCI (%)
1	144,996	1.069	-10.58	
1	204,076	1.073	-4.96	
1	349927	1.108	-1.50	1.18
2	144,996	2.249	-27.76	
2	205,900	2.385	-14.17	
2	352,277	2.476	-5.06	1.64
3	144,725	4.281	-14.68	
3	206,852	4.418	-1.04	
3	347,665	4.428	-0.02	0.006

C Deposition velocity of dust particles on leaves of *H. helix*

The following figures show the results, in terms of the deposition velocity (v_d, m s^{-1}) of different models used to simulate PM deposition onto leaves of H. helix.

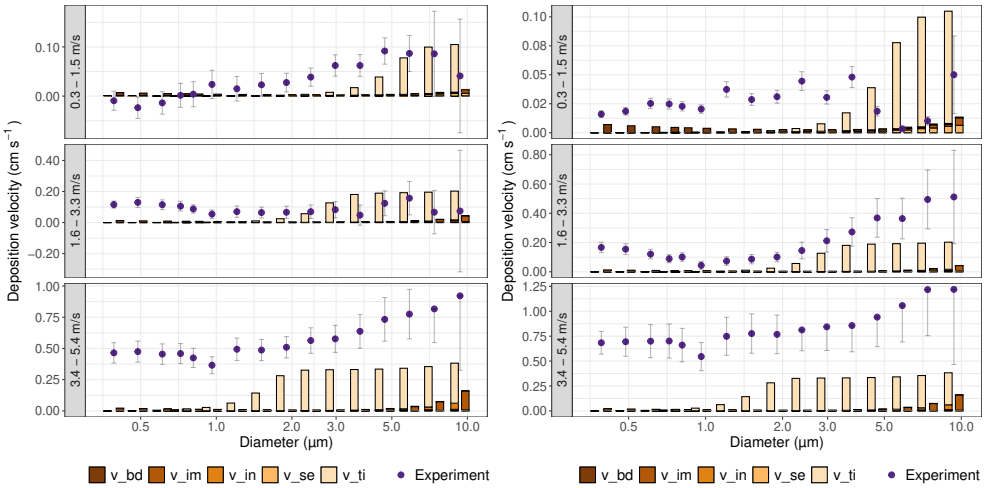

Fig. 11 Measured total v_d (m s^{-1}, bullets) and modelled deposition velocity (m s^{-1}, bar plot) of each PM deposition mechanisms (1^{st} bar = Petroff model, 2^{nd} bar = Zhang model) for an incoming PM_{10} concentration of 100 (left) and 150 µg m^{-3} (right).

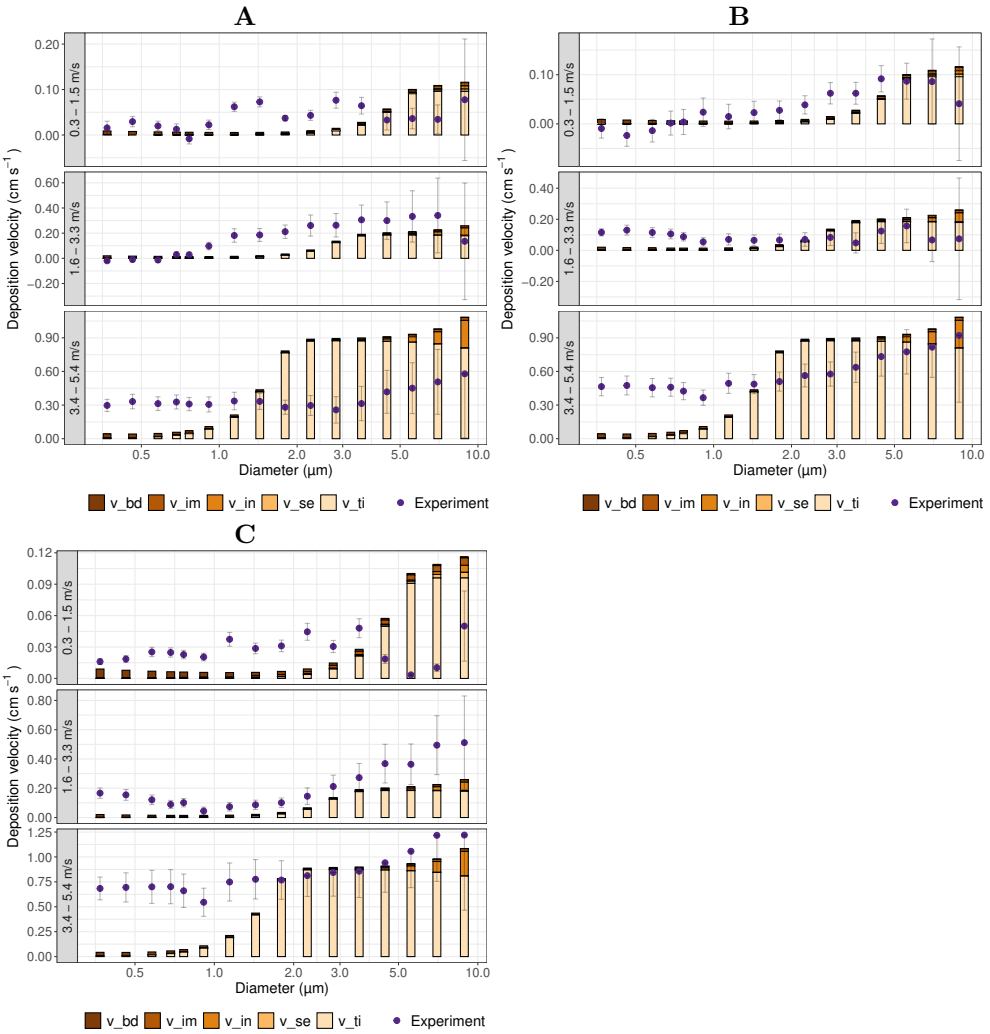

Fig. 12 Measured total v_d (m s^{-1}, bullets) and modelled deposition velocity (m s^{-1}, bar plot) of each PM deposition mechanisms with the modified model combining the model of Zhang and Petroff for an incoming PM_{10} concentration of 50 (A), 100 (B) and 150 µg m^{-3} (C).

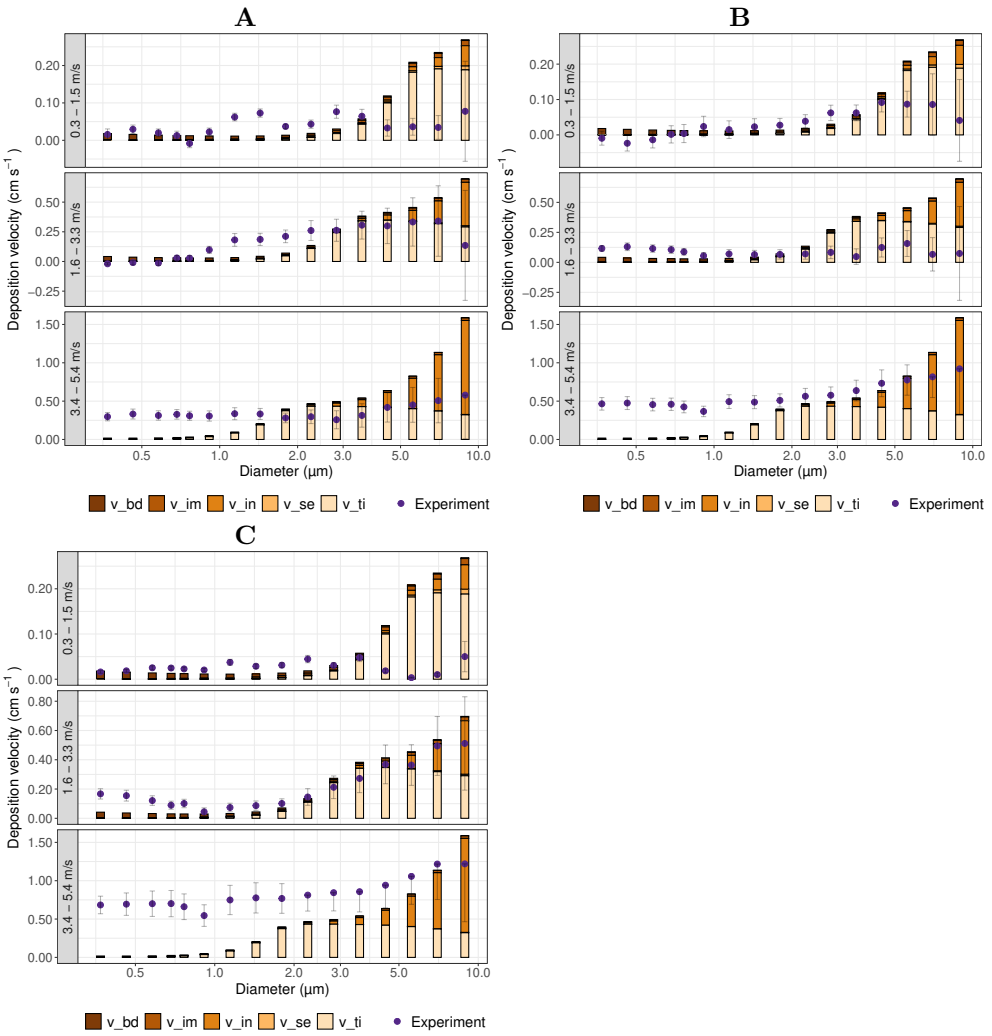

Fig. 13 Measured total v_d (m s^{-1}, bullets) and modelled deposition velocity (m s^{-1}, bar plot) of each PM deposition mechanisms with the modified model with a turbulent Stokes number for an incoming PM_{10} concentration of 50 (A), 100 (B) and 150 µg m^{-3} (C).

References

12103-1 (2016) Road vehicles - test contaminants for filter evaluation - part 1: Arizona test dust. Tech. rep.

Abhijith KV, Kumar P, Gallagher J, et al (2017) Air pollution abatement performances of green infrastructure in open road and built-up street canyon environments – a review. Atmospheric Environment 162:71–86. https://doi.org/10.1016/j.atmosenv.2017.05.014

Amicarelli A, Alessandrini S, Agate G, et al (2021) A dry deposition scheme for particulate matter coupled with a well-known lagrangian stochastic model for pollutant dispersion. Environmental Fluid Mechanics 21(2):433–463. https://doi.org/10.1007/s10652-021-09780-y

Beckett KP, Freer-Smith PH, Taylor G (2000) The capture of particulate pollution by trees at five contrasting urban sites. Arboricultural Journal 24(2-3):209–230. https://doi.org/10.1080/03071375.2000.9747273

Burtscher H (2005) Physical characterization of particulate emissions from diesel-engines: a review. Aerosol Science 36:896–932. https://doi.org/doi:10.1016/j.jaerosci.2004.12.001

Chang JC, Hanna SR (2004) Air quality model performance evaluation. Meteorology and atmospheric physics 87:167–196. https://doi.org/10.1007/s00703-003-0070-7

Dulbari D, Santosa E, Sulistyono E, et al (2017) Adaptation of wetland rice to extreme weather. Journal of Tropical Crop Science 4(2):70–77. https://doi.org/10.29244/jtcs.4.2.70-77

EEA (2022) Air quality in europe 2022. Tech. rep., European Environmental Agency, https://doi.org/10.2800/488115

Freer-Smith PH, El-Khatib AA, Taylor G (2004) Capture of particulate pollution by trees: A comparison of species typical of semi-arid areas (*Ficus Nitida* and *Eucalyptus Globulus*) with european and north american species. Water, Air, and Soil Pollution 155:173–187. https://doi.org/10.1023/B:WATE.0000026521.99552.fd

Freer-Smith PH, Beckett KP, Taylor G (2005) Deposition velocities to sorbus aria, acer campestre, populus deltoides × trichocarpa 'beaupré', pinus nigra and × cupressocyparis leylandii for coarse, fine and ultra-fine particles in the urban environment. Environmental Pollution 133(1):157–167. https://doi.org/10.1016/j.envpol.2004.03.031

Gromke C, Blocken B (2015) Influence of avenue-trees on air quality at the urban neighborhood scale. part i: Quality assurance studies and turbulent schmidt number analysis for RANS CFD simulations. Environmental Pollution 196:214–223. https://doi.org/10.1016/j.envpol.2014.10.016

Hair JF, Black JWC, Babin BJ, et al (2014) Multivariate Data Analysis, seventh edition edn. Pearson Education Limited

Hashad K, Yang B, Gallagher J, et al (2023) Impact of roadside conifers vegetation growth on air pollution mitigation. Landscape and Urban Planning 229:104594. https://doi.org/10.1016/j.landurbplan.2022.104594

Huang CW, Lin MY, Khlystov A, et al (2013) The effects of leaf area density variation on the particle collection efficiency in the size range of ultrafine particles (UFP). Environmental Science & Technology 47(20):11607–11615. https://doi.org/10.1021/es4013849

Huang CW, Lin MY, Khlystov A, et al (2015) The effects of leaf size and micro-roughness on the branch-scale collection efficiency of ultrafine particles. Journal of Geophysical Research: Atmospheres 120(8):3370–3385. https://doi.org/10.1002/2014jd022458

Hwang HJ, Yook SJ, Ahn KH (2011) Experimental investigation of submicron and ultrafine soot particle removal by tree leaves. Atmospheric Environment 45(38):6987–6994. https://doi.org/10.1016/j.atmosenv.2011.09.019

Janhäll S (2015) Review on urban vegetation and particle air pollution – deposition and dispersion. Atmospheric Environment 105:130–137. https://doi.org/10.1016/j.atmosenv.2015.01.052

Katata G, Kajino M, Matsuda K, et al (2014) A numerical study of the effects of aerosol hygroscopic properties todry deposition on a broad-leaved forest. Atmospheric environment 97:501–510. https://doi.org/10.1016/j.atmosenv.2013.11.028

Koch K, Samson R, Denys S (2019) Aerodynamic characterisation of green wall vegetation based on plant morphology: An experimental and computational fluid dynamics approach. Biosystems Engineering 178:34–51. https://doi.org/10.1016/j.biosystemseng.2018.10.019

Kwon HS, Ryu MH, Carlsten C (2020) Ultrafine particles: unique physicochemical properties relevant to health and disease. Experimental & Molecular Medicine 52(3):318–328. https://doi.org/10.1038/s12276-020-0405-1

Legg R (2017) Fluid Flow: General Principles, Elsevier, pp 225–257. https://doi.org/10.1016/b978-0-08-101123-2.00013-3

Leonard RJ, McArthur C, Hochuli DF (2016) Particulate matter deposition on roadside plants and the importance of leaf trait combinations. Urban Forestry & Urban

Greening 20:249–253. https://doi.org/10.1016/j.ufug.2016.09.008

Lin M, Katul GG, Khlystov A (2012) A branch scale analytical model for predicting the vegetation collection efficiency of ultrafine particles. Atmospheric Environment 51:293–302. https://doi.org/10.1016/j.atmosenv.2012.01.004

Maricq MM (2014) Examining the relationship between black carbon and soot in flames and engine exhaust. Aerosol Science and Technology 48(6):620–629. https://doi.org/10.1080/02786826.2014.904961

Mattis SA, Dawson CN, Kees CE, et al (2012) Numerical modeling of drag for flow through vegetated domains and porous structures. Advances in Water Resources 39:44–59. https://doi.org/10.1016/j.advwatres.2012.01.002

Moore RH, Ziemba LD, Dutcher D, et al (2014) Mapping the operation of the miniature combustion aerosol standard (mini-CAST) soot generator. Aerosol Science and Technology 48(5):467–479. https://doi.org/10.1080/02786826.2014.890694

Moran SM, Pardyjak ER, Veranth JM (2013) Understanding the role of grid turbulence in enhancing PM_10 deposition: Scaling the stokes number with r_λ. Physics of Fluids 25(11):115103. https://doi.org/10.1063/1.4829451

Muhammad S, Wuyts K, Samson R (2019) Atmospheric net particle accumulation on 96 plant species with contrasting morphological and anatomical leaf characteristics in a common garden experiment. Atmospheric Environment 202:328–344. https://doi.org/10.1016/j.atmosenv.2019.01.015

Ould-Dada Z (2002) Dry deposition profile of small particles within a modelspruce canopy. Science of the Total Environment 286:83–96. https://doi.org/10.1016/S0048-9697(01)00965-2

Pappa V, Bouris D, Theurer W, et al (2023) A wind tunnel study of aerodynamic effects of façade and roof greening on air exchange from a cubic building. Building and Environment 231:110023. https://doi.org/10.1016/j.buildenv.2023.110023

Paull NJ, Irga PJ, Torpy FR (2019) Active botanical biofiltration of air pollutants using australian native plants. Air Quality, Atmosphere & Health 12:1427–1439. https://doi.org/10.1007/s11869-019-00758-w

Pérez G, Coma J, Sol S, et al (2017) Green facade for energy savings in buildings: The influence of leaf area index and facade orientation on the shadow effect. Applied Energy 187:424–437. https://doi.org/10.1016/j.apenergy.2016.11.055

Petroff A, Zhang L (2010) Development and validation of a size-resolved particle dry deposition scheme for application in aerosol transport models. Geoscientific Model Development 3(2):753–769. https://doi.org/10.5194/gmd-3-753-2010

Petroff A, Zhang L, Pryor SC, et al (2009) An extended dry deposition model for aerosols onto broadleaf canopies. Journal of Aerosol Science 40(3):218–240. https://doi.org/10.1016/j.jaerosci.2008.11.006

Price TA, Stoll R, Veranth JM, et al (2017) A wind-tunnel study of the effect of turbulence on pm_10 deposition onto vegetation. Atmospheric Environment 159:117–125. https://doi.org/10.1016/j.atmosenv.2017.03.043

Pryor SC, Gallagher M, Sievering H, et al (2008) A review of measurement and modelling results of particle atmosphere–surface exchange. Tellus B: Chemical and Physical Meteorology 60(1):42–75. https://doi.org/10.1111/j.1600-0889.2007.00298.x

Roach PE (1987) The generation of nearly isotropicturbulence by means of grids. Heath and flow 8(2):82–92. https://doi.org/10.1016/0142-727X(87)90001-4

Roegiers J, Denys S (2019) CFD-modelling of activated carbon fibers for indoor air purification. Chemical Engineering Journal 365:80–87. https://doi.org/10.1016/j.cej.2019.02.007

Saffaripour M, Tay LL, Thomson KA, et al (2017) Raman spectroscopy and TEM characterization of solid particulate matter emitted from soot generators and aircraft turbine engines. Aerosol Science and Technology 51(4):518–531. https://doi.org/10.1080/02786826.2016.1274368

Sakamoto Y, Ishiguro M, Kitagawa G (1986) Akaike information criterion statistics. Mathematics and its Applications, Springer Netherlands

Shen JW, Cui PY, Huang YD, et al (2022) New insights into quantifying deposition and aerodynamic characteristics of PM2.5 removal by different tree leaves. Air Quality, Atmosphere & Health 15(8):1341–1356. https://doi.org/10.1007/s11869-022-01157-4

Sogachev A (2009) A note on two-equation closure modelling of canopy flow. Boundary-Layer Meteorology 130(3):423–435. https://doi.org/10.1007/s10546-008-9346-2

Steffens JT, Wang YJ, Zhang KM (2012) Exploration of effects of a vegetation barrier on particle size distributions in a near-road environment. Atmospheric Environment 50:120–128. https://doi.org/10.1016/j.atmosenv.2011.12.051

Tomson M, Kumar P, Barwise Y, et al (2021) Green infrastructure for air quality improvement in street canyons. Environment International 146:106288. https://doi.org/10.1016/j.envint.2020.106288

Tong Z, Baldauf RW, Isakov V, et al (2016) Roadside vegetation barrier designs to mitigate near-road air pollution impacts. Science of The Total Environment 541:920–927. https://doi.org/10.1016/j.scitotenv.2015.09.067

Wang H, Maher BA, Ahmed IAM, et al (2019) Efficient removal of ultrafine particles from diesel exhaust by selected tree species: Implications for roadside planting for improving the quality of urban air. Environmental Science & Technology 53(12):6906–6916. https://doi.org/10.1021/acs.est.8b06629

Weerakkody U, Dover JW, Mitchell P, et al (2017) Particulate matter pollution capture by leaves of seventeen living wall species with special reference to rail-traffic at a metropolitan station. Urban Forestry & Urban Greening 27:173–186. https://doi.org/10.1016/j.ufug.2017.07.005

WHO (2021) Who global air quality guidelines. particulate matter (pm2.5 and pm10), ozone, nitrogen dioxide, sulfur dioxide and carbon monoxide. Tech. rep., World Health Organisation

Wilcox DC (2008) Formulation of the k - ω turbulence model revisited. AIAA Journal 46(11). https://doi.org/10.2514/1.36541

Ysebaert T, Koch K, Samson R, et al (2021) Green walls for mitigating urban particulate matter pollution - a review. Urban Forestry & Urban Greening 59:127014. https://doi.org/10.1016/j.ufug.2021.127014

Ysebaert T, Samson R, Denys S (2022) Parameterisation of the drag effect of climbers depending on wind speed and LAD. Sustainable Cities and Society 84:103979. https://doi.org/10.1016/j.scs.2022.103979

Zeng F, Lei C, Liu J, et al (2020) CFD simulation of the drag effect of urban trees: Source term modification method revisited at the tree scale. Sustainable Cities and

Society 56:102079. https://doi.org/10.1016/j.scs.2020.102079

Zhang L, Gong S, Padro J, et al (2001) A size-segregated particle dry deposition scheme for an atmospheric aerosol module. Atmospheric Environment 35:549–560. https://doi.org/10.1016/S1352-2310(00)00326-5

Šíp V, Beneš L (2017) Dry deposition model for a microscale aerosol dispersion solver based on the moment method. Journal of Aerosol Science 107:107–122. https://doi.org/10.1016/j.jaerosci.2017.02.010